Random-phase approximation of core-electron scattering in solids

K. Nuroh*
Department of Mathematical Sciences, Kent State University, Salem, Ohio 44460, USA
(Received 13 November 2003; revised manuscript received 23 June 2004; published 12 November 2004)

The interference between bound-bound transition and bound-free transition in an electron-impact excitation of a core-electron in systems with narrow bands is discussed within the context of diagrammatic perturbation theory. The earlier treatment of the phenomenon in terms of autoionization and characteristic widths of the core-hole via perturbation ladder diagrams is extended to include ring diagrams as well, in random-phase approximation (RPA). The associated characteristic line shape for the intensity of the inelastically scattered electrons is formulated in terms of Fano line shape parameters, and theory is compared with electron-energy loss measurements for metallic La and Ce.

DOI: 10.1103/PhysRevB.70.205115 PACS number(s): 71.27.+a, 71.28.+d, 79.20.Fv, 79.20.Uv

I. INTRODUCTION

The response of electrons to some external perturbation in a metal in the Fermi-sea picture is usually adequately analyzed via linear response formalism or the Kubo[1] formula approach, which in turn requires the evaluation of a susceptibility tensor in general. If for example one is interested in the transport properties of the solid, then the susceptibility is defined in terms of the current-current correlation function. Embedded in the susceptibility are various interactions that introduce electron correlations of the system. One way of evaluating the susceptibility is the use of diagrammatic perturbation theory. An exact evaluation of the susceptibility is impossible within this approach. Rather an approximation of some sort is resorted to depending on the physical property of interest. For an extended system, it is usually sufficient to describe many of the physical properties with the knowledge of the band structure of the solid. To evaluate the approximate susceptibility in this Coulomb long-range interaction limit is equivalent to summing a particular set of bubble or ring diagrams describing the repeated electron-hole interactions in the random-phase approximation (RPA).[2] However, if electron correlations are to be properly accounted for, particularly if the interactions involve core electrons, then it is necessary to include the atomic structure of the solid in some fashion. Such an approach was taken, for example, in the Hubbard[3] model in order to unveil the dominant short-range part of the Coulomb interactions responsible for the instabilities in *d*-electrons in transition metals. To evaluate the susceptibility in the Hubbard interaction model is equivalent to considering a generalized Hartree-Fock approximation describing the repeated electron-hole interactions resulting in a set of ladder diagrams that is summed in the RPA.[4]

The foregoing preamble establishes the fact that whenever the RPA is invoked, the ladder and ring diagrams must in principle be considered on the same footing. Depending on the observable quantity of interest however, one subset of diagrams may be more relevant than the other. For example, the RPA result for the electron correlation energy in the jellium model of a solid employs a series of ring diagrams.[5] On the other hand, in the calculation of the ground state energy of an imperfect Fermi gas modeled as a dilute gas interacting with strong short-range repulsive potentials, contributions from two-particle scattering processes necessitate the summation of ladder diagrams.[6]

The RPA has also found successful application in the study of the electronic structure of some highly polarizable atomic and solid-state systems. Beginning with the work of Amusia, Cherepkov, and Chernysheva[7] in the discussion of the photoionization of noble-gas atoms using the diagrammatic random-phase approximation with exchange (RPAE), Wendin[8] used RPA ring diagrams to discuss the photoionization cross sections of xenon. He later extended the same RPA diagrammatic approach to calculate photoionization cross sections of metallic lanthanum, thorium, and uranium using local density functional-based approximated (LDA) orbitals for the wave functions.[9,10] Calculations based on the RPA approach usually yield results that mimic those based on time-dependent density-functional approximation (TDLDA). The TDLDA calculations for barium and cerium by Zangwill and Soven[11] on one hand, and for the barium ionized series on the other by Nuroh, Stott, and Zaremba[12] compared with the RPA calculations of Ref. 8 exemplify the above assertion. Indeed, the uncanny similarity in the numerical photoabsorption cross-section results for xenon, barium, and cerium using RPA and TDLDA separately, led Nuroh[13] to formally demonstrate the mathematical equivalence between the ring diagram-based RPA and the TDLDA as far as calculations of dynamic polarizability of atoms are concerned.

The ladder-based RPA has been used to discuss the 4*d*-subshell electron energy-loss spectra (EELS) in lanthanum and cerium metals.[14] There, the successive electron-hole pair interactions have been formulated in terms of an effective interaction through the introduction of a self-energy in a Dyson-type equation so as to make comparative spectral analysis between 3*d* and 4*d* EELS apparent.

In this paper, we extend the above earlier discussion to include ring-based RPA as well. The formulation will be symmetric in the introduction of self-energies for both the ring and ladder diagrams. Moreover, unlike the earlier discussion, the self-energies will be quadratic in the electron-hole pair bare interactions, albeit the interactions appear differently in the respective self-energies. The obvious advantage to such decomposition is that it allows for transparent comparison in the interactions involved in the ring and ladder diagrams, as well as the relative intensities emanating from the two respective excitation channels.

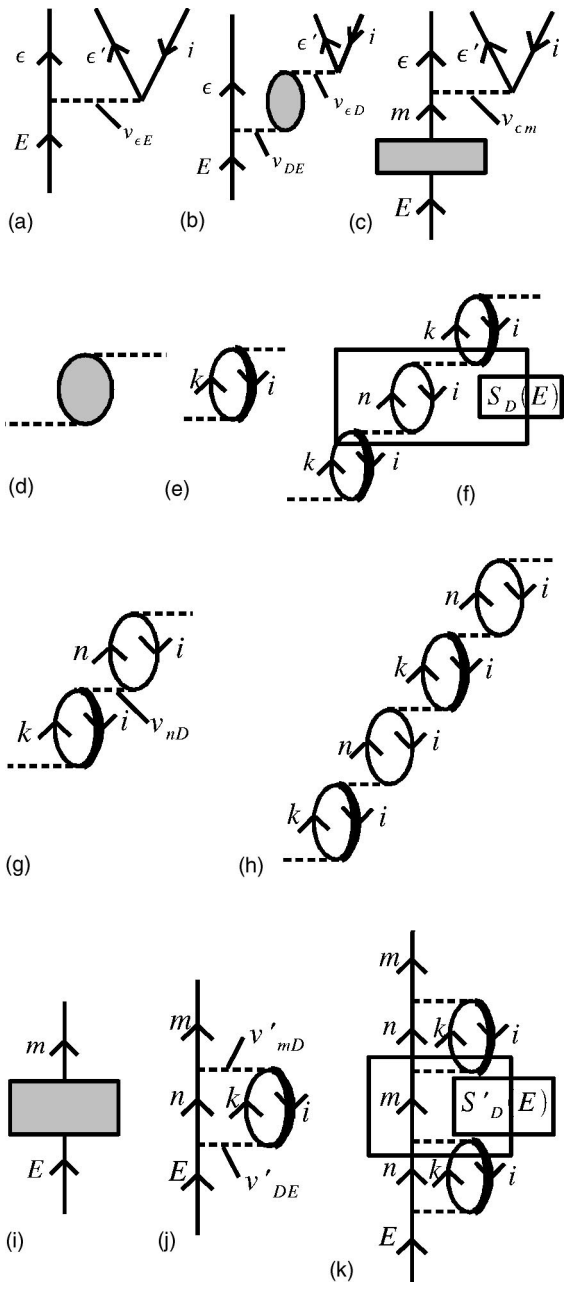

FIG. 1. Amplitude diagrams made up of (a): the basic excitation amplitude; (b), (d)–(h) the resonant contributions from the ring diagrams; (c), (i)–(k) the resonant contributions from ladder diagrams.

II. FORMULATION

We employ Raleigh-Schrödinger perturbation theory for the description of the electron impact excitation processes. In the one-electron picture, and incident electron of energy E scatters to a state $|\epsilon\rangle$ above the Fermi level of the metal while a core electron of state label $|\underline{i}\rangle$ is excited to a state $|\epsilon'\rangle$ above the Fermi level. (An underlined state label means that the state propagates as a hole.) The Coulomb interaction responsible for this scattering process is represented by the amplitude graph of Fig. 1(a) in which the dashed line indicates the Coulomb interaction matrix element labeled $V_{\epsilon E}$. Figures 1(b) and 1(c) describe the general structure of resonant contributions from ring and ladder graphs to the basic excitation amplitude of Fig. 1(a). They may be viewed as an initial state $|E\rangle$ coupling to a two-particle and one-hole final state $|\underline{i}\epsilon'\epsilon\rangle$ consistent with Fig. 1(a). We note in passing that Figs. 1(b) and 1(d)–1(h) that constitute the ring graphs are corrections to the ladder graphs of Figs. 1(a), 1(c), and 1(i)–1(k) used in the earlier treatment.[14]

In Fig. 1(b), V_{DE} is a Coulomb interaction matrix element of state $|E\rangle$ and a discrete state involving the core-hole $|\underline{i}\rangle$ i.e., the state $|\underline{i}k\epsilon\rangle$. The shaded ring graph plus the interaction vertex lines in Fig. 1(b) is reconstituted in Fig. 1(d). Figure 1(d) represents all possible ring graph insertions that begin with the Coulomb interaction matrix element or the interaction vertex line V_{DE} and end up with the interaction vertex line $v_{\epsilon D}$. In other words, we are looking at infinite order perturbation in interaction between the discrete state $|\underline{i}k\epsilon\rangle$ and the continuum state $|\underline{i}n\epsilon\rangle$, and such a basic interaction between the two states is represented by Fig. 1(b). (A thick hole-line indicates the renormalized orbital that gives rise to characteristic decay width of the state $|\underline{i}\rangle$.) The decomposition of Fig. 1(d) is made up of all the graphs of Figs. 1(e)–1(h). Further, a regrouping of the ring graphs is made to consist of those that begin and end with a thick hole-line or renormalized state (i.e., those containing *odd* number of ring graphs—Fig. 1(e), Fig. 1(f), and higher orders), and those that begin with a renormalized discrete state and end with a continuum state (i.e., those containing *even* number of ring graphs—Fig. 1(g), Fig. 1(h), and higher orders. In the above decomposition $S_D(E)$ indicates a self-energy of the discrete state.

The shaded rectangular graph in Fig. 1(c) is reconstituted in Fig. 1(i) that is made up of graphs of Figs. 1(j) and 1(k) and higher orders. Figure 1(j) is the basic or lowest order ladder graph to Fig. 1(i). In Fig. 1(j), v'_{DE} is a Coulomb interaction matrix element between the state $|E\rangle$ and the discrete state $|\underline{i}kn\rangle$. Notice that the interaction matrix elements v_{DE} and v'_{DE} differ not only because the orbitals $|\epsilon\rangle$ and $|n\rangle$ for the respective discrete states $|\underline{i}k\epsilon\rangle$ and $|\underline{i}jn\rangle$ in which they appear differ, but also in that they would have different angular factors. Here $S'_D(E)$ in Fig. 1(k) is the self-energy of the discrete state for the ladder diagrams. We note in passing that Figs. 1(a), 1(j), and 1(k) were the graphs used essentially in the discussion of the EEL spectra of lanthanum and cerium in the previous work.[14] The present work is therefore an extension of that work with the inclusion of contribution from ring graphs. We may therefore say that the analysis described thus far is a simpler derivation of the more complicated multichannel Fano-type calculations that have been used variously to discuss photoionization cross sections of some materials.[15–17]

First, we consider the contribution to the excitation amplitude that emanates from the ring graphs and the nonresonant graph (Fig. 1(a)) and denote this by $a(E)$. The nonresonant graph, Fig. 1(a), was part of the ladder graphs in Ref. 14. Since it is the basic interaction, we make it part of the ring graphs in the present formulation. Subsequently, if the ring graphs are to be neglected, we simply set $v_{DE}=0$, or equivalently, $\gamma=0$ in Eq. (19) to be consistent with the earlier results that makes Fig. 1(a) part of the ladder graphs. Thus from Figs. 1(a) and 1(b) and Figs. 1(d)–1(h), we get

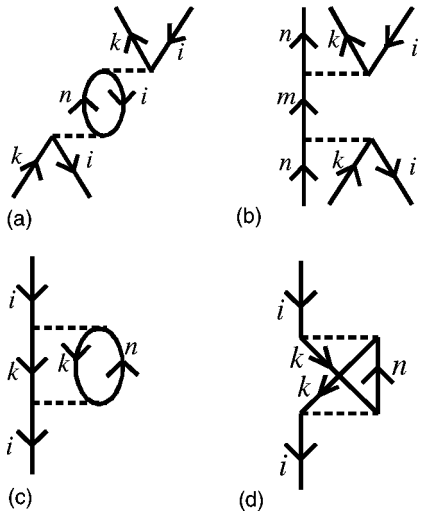

FIG. 2. Self-energy diagrams made up of (a) the self-energy insertion for ring diagrams, (b) the self-energy insertion for ladder diagrams, (c) Coulomb interaction for the characteristic decay of the discrete state, (d) exchange contribution to (c).

$$
\begin{aligned}
a(E) &= \left[v_{\epsilon E} + \frac{v_{\epsilon D} v_{DE}}{E_D - E} + \frac{v_{DE}}{E_D - E}\left(\frac{S_D(E)}{E_D - E}\right) v_{\epsilon D} + \cdots \right] \\
&\quad + \left[\frac{v_{DE}}{E_D - E} \sum_n \frac{v_{\epsilon n} v_{nD}}{E_n - E - i\delta} \right. \\
&\quad \left. + \frac{v_{DE}}{E_D - E}\left(\frac{S_D(E)}{E_D - E}\right) \sum_n \frac{v_{\epsilon n} v_{nD}}{E_n - E - i\delta} + \cdots \right] \\
&= v_{\epsilon E} + \frac{v_{\epsilon D} v_{DE}}{E_D - E}\left\{ 1 + \left(\frac{S_D(E)}{E_D - E}\right) + \cdots \right\} \\
&\quad + \frac{v_{DE}}{E_D - E} \sum_n \frac{v_{\epsilon n} v_{nD}}{E_n - E - i\delta}\left\{ 1 + \left(\frac{S_D(E)}{E_D - E}\right) + \cdots \right\},
\end{aligned}
\tag{1}
$$

with the following definitions for E_D and $S_D(E)$:

$$
E_D = \epsilon + E_k - \Sigma_i(E), \tag{2}
$$

$$
S_D(E) = \sum_n \frac{v_{nD}^2}{E_n - E - i\delta} = \sum_n{}' \frac{v_{nD}^2}{E_n - E} + i\pi v_{ED}^2. \tag{3}
$$

The interacting self-energy $S_D(E)$ is represented by the angular momentum diagram in Fig. 2(a) for the ring graphs,[8] while Fig. 2(b) is the corresponding diagram for the self-energy $S_D'(E)$ for the ladder graphs[14] to be considered later. In Eq. (3) and hereafter, a prime on a summation sign means that a principal part summation/integration is implied. In Eq. (2), Σ_i is the self-energy of the core state defined by

$$
\begin{aligned}
\Sigma_i(E) &= \sum_n \frac{v_n^2}{E_n - E_k - E_k - E - i\delta} \\
&= \sum_n{}' \frac{v_n^2}{E_n - E_k - E_k - E} + i\pi v_{E-2E_k}^2.
\end{aligned}
\tag{4}
$$

Hereafter, we will use the shortened notation v_E^2 for $v_{E-2E_k}^2$ in Eq. (4) above.

The Coulomb interaction matrix element v_n^2 is obtained from the self-energy graphs of Figs. 2(c) and 2(d). Figure 2(c) is a Feynman diagram of the core-hole self-energy $\Sigma_i(E)$,[18] while Fig. 2(d) is its corresponding exchange diagram, constructed using angular momentum graphical techniques.[19] If we introduce an effective interaction matrix element $V_{\epsilon D}(E)$ by the equation

$$
\begin{aligned}
V_{\epsilon D}(E) &= v_{\epsilon D} + \sum_n \frac{v_{\epsilon n} v_{nD}}{E_n - E - i\delta} \\
&= v_{\epsilon D} + \sum_n{}' \frac{v_{\epsilon n} v_{nD}}{E_n - E} + i\pi v_{\epsilon E} v_{ED},
\end{aligned}
\tag{5}
$$

then by summing to infinity the terms in the two curly brackets in Eq. (1) which form geometric series, we get the following compact expression for the excitation amplitude:

$$
a(E) = v_{\epsilon E} + \frac{V_{\epsilon D}(E) v_{DE}}{E_D - S_D(E) - E}. \tag{6}
$$

Further, if we introduce the Fano[20] line width parameters $q(E)$ and $\eta(E)$ by

$$
q(E) = \frac{\mathrm{Re}\, V_{\epsilon D}(E)}{\mathrm{Im}\, V_{\epsilon D}(E)} = \left(v_{\epsilon D} + \sum_n{}' \frac{v_{\epsilon n} v_{nD}}{E_n - E} \right) / \pi v_{\epsilon E} v_{ED}, \tag{7a}
$$

$$
\eta(E) = -\frac{\mathrm{Re}(E - S_D(E) - E)}{\mathrm{Im}(E - S_D(E) - E)}, \tag{7b}
$$

and define the autoionizing, characteristic, and total line width parameters, respectively, by Γ_a, Γ_c, and Γ_t,[14] through the equations

$$
\Gamma_a/2\pi = v_{ED}^2, \quad \Gamma_c/2\pi = v_E^2, \quad \Gamma_t = \Gamma_a + \Gamma_c, \tag{8}
$$

then with some algebra, the excitation amplitude reduces to the simpler form

$$
a(E) = v_{\epsilon E}\left[1 + \frac{\Gamma_a}{\Gamma_t}\left\{ \frac{q + i}{\eta - i} \right\} \right]. \tag{9}
$$

The matrix element v_E^2 that appears in Eq. (8) is defined in Eq. (4) and the statement after the equation.

The contribution to the excitation amplitude arising from the ladder graphs is denoted by $b(E)$. Thus from Fig. 1(c) and Figs. 1(i)–1(k), we get

$$b(E) = \frac{v'_{DE}}{E'_D - E}\sum_m \frac{v'_{mD}v_{\epsilon m}}{E'_m - E - i\delta} + \frac{v'_{DE}}{E'_D - E}\frac{S'_D(E)}{E'_D - E}\sum_m \frac{v'_{mD}v_{\epsilon m}}{E'_m - E - i\delta} + \cdots = \frac{v'_{DE}}{E'_D - E}\sum_m \frac{v'_{mD}v_{\epsilon m}}{E'_m - E - i\delta}\left[1 + \frac{S'_D(E)}{E'_D - E} + \cdots\right], \tag{10}$$

where

$$E'_D = E_n + E_k - \Sigma_i(E). \tag{11}$$

By introducing the self-energy $S'_D(E)$ and an effective interaction $V'_{D\epsilon}(E)$ through the equations

$$S'_D(E) = \sum_m \frac{v'^2_{ED}}{E_m - E - i\delta} = \sum_m{}' \frac{v'^2_{ED}}{E_m - E} + i\pi v'^2_{ED}, \tag{12}$$

$$V'_{D\varepsilon} = \sum_m \frac{v'_{mD}v_{\epsilon m}}{E_m - E - i\delta} = \sum_m{}' \frac{v'_{mD}v_{\epsilon m}}{E_m - E} + i\pi v'_{ED}v_{\epsilon E}, \tag{13}$$

and summing the infinite geometric series in the square brackets of Eq. (10) gives a simpler form for $b(E)$ as

$$b(E) = \frac{v'_{DE}V'_{D\varepsilon}(E)}{E'_D - S'_D(E) - E}. \tag{14}$$

Once more, we introduce new Fano line width parameters

$$q'(E) = \frac{\mathrm{Re}\, V'_{D\epsilon}(E)}{\mathrm{Im}\, V'_{D\varepsilon}} = \sum_m{}' \frac{v'_{mD}v_{\epsilon m}}{E_m - E}\Big/\pi v'_{ED}v_{\epsilon E} \tag{15a}$$

$$\eta'(E) = -\frac{\mathrm{Re}(E'_D - S'_D(E) - E)}{\mathrm{Im}(E'_D - S'_D(E) - E)}. \tag{15b}$$

Again if we introduce the autoionizing, characteristic, and total line widths, respectively, by Γ'_a, Γ'_c, and Γ'_t for the new channel by the equations

$$\Gamma'_a/2\pi = v'^2_{ED}, \quad \Gamma'_c/2\pi = v^2_E = \Gamma_c/2\pi, \quad \Gamma'_t = \Gamma'_a + \Gamma'_c, \tag{16}$$

then $b(E)$ takes on the form,

$$b(E) = v_{\epsilon E}\frac{\Gamma'_a}{\Gamma'_t}\left\{\frac{q' + i}{\eta' - i}\right\}. \tag{17}$$

Again, the matrix element v^2_E that appears in Eq. (16) is defined in Eq. (4). Notice that the characteristic line width is the same for both the ring and ladder channels as indicated in Eq. (16). Finally, by introducing the dimensionless parameters γ and γ' as ratios of the autoionizing to the total line widths in the respective channels by

$$\gamma = \Gamma_a/\Gamma_t, \ \gamma' = \Gamma'_a/\Gamma'_t. \tag{18}$$

Equations (9) and (17) can be combined to give the total excitation amplitude $A(E)$ that is the sum of $a(E)$ and $b(E)$ as

$$A(E) = v_{\epsilon E}\left[1 + \gamma\left\{\frac{q + i}{\eta - i}\right\} + \gamma'\left\{\frac{q' + i}{\eta' - i}\right\}\right]. \tag{19}$$

Each q-value ultimately gives rise to a partial excitation cross section as a function of the energy lost by the incident electron to the system. From Eqs. (7b) and (15b) we find that

$$\Delta\eta = \eta(E) - \eta'(E) = \frac{2\,\mathrm{Re}(E_D - S_D(E) - E)}{\Gamma_t} - \frac{2\,\mathrm{Re}(E'_D - S'_D(E) - E)}{\Gamma'_t}. \tag{20}$$

I will return to this general expression later in the article. It is useful to first examine some limiting cases. First setting $\eta' = \eta$ in Eq. (19) gives $A(E)$ as

$$A(E) = v_{\epsilon E}\left[\frac{(\eta + \gamma q + \gamma' q') + (\gamma + \gamma' - 1)i}{\eta - i}\right]. \tag{21}$$

The scattering intensity $I(E)$ is proportional to the square of the absolute value of the excitation amplitude. Thus

$$I(E) \sim |A(E)|^2 = v^2_{\epsilon E}\left[\frac{(\eta + \gamma q + \gamma' q')^2 + (\gamma + \gamma' - 1)^2}{\eta^2 + 1}\right]. \tag{22}$$

We consider different physical scenarios that would arise from Eq. (22). First we set $\gamma' = 0$ to exclude contributions from ladder graphs, and $\gamma = 1$, appropriate for La when $\Gamma_c = 0$. In such a situation the scattering intensity becomes (where the subscript R denotes ring)

$$I_R(E) = v^2_{\epsilon E}[(\eta + q)^2/(\eta^2 + 1)]. \tag{23}$$

This is essentially a Fano line profile excluding the nonresonant interaction matrix $v^2_{\epsilon E}$. If we still exclude the contributions from the ladder graphs by demanding that $\gamma \neq 1$, then the scattering intensity becomes (appropriate for Ce)

$$I_R(E) = v^2_{\epsilon E}\left[\frac{(\eta + \gamma q)^2 + (\gamma - 1)^2}{\eta^2 + 1}\right]. \tag{24}$$

Excluding contributions from ring graphs, we have to set $\gamma = 0$. Then with $\gamma' = 1$ ($\Gamma'_c = 0$), the scattering intensity becomes (where the subscript L denotes ladder), and appropriate for La,

$$I_L(E) = v^2_{\epsilon E}[(\eta + q')^2/(\eta^2 + 1)]. \tag{25}$$

This is the result obtained in form in the earlier work, albeit q' is defined in terms of different matrix elements. Finally, by still excluding the ring graphs but now demanding that $\gamma' \neq 1$, the scattering intensity takes on the form (appropriate for Ce),

$$I_L(E) = v^2_{z\epsilon E}\left[\frac{(\eta + \gamma' q')^2 + (\gamma' - 1)^2}{\eta^2 + 1}\right]. \tag{26}$$

In a situation in which $\Delta\eta$ is not approximately equal to zero, then we have to set $\eta' = \eta - \Delta\eta$. In such a case, the excitation amplitude of Eq. (19) has to be modified to take its complete form $A_C(E)$ given by

$$A_C(E) = v_{\epsilon E}\left[1 + \gamma\left\{\frac{q+i}{\eta - i}\right\} + \left\{\frac{q'+i}{\eta - \Delta\eta - i}\right\}\right]. \quad (27)$$

By taking the square of the absolute value of the above, we get the complete scattering intensity $I_C(E)$ as

$$I_C(E) \sim v_{\epsilon E}^2\left\{\left[\frac{\gamma(\eta+q)}{\eta^2+1} + \frac{\gamma' q' + \gamma'(\eta - \Delta\eta)}{(\eta - \Delta\eta)^2 + 1}\right]^2 + \left[\frac{\eta^2 + \eta\gamma q - \gamma + 1}{\eta^2+1} + \frac{\gamma' q'(\eta - \Delta\eta) - \gamma'}{(\eta - \Delta\eta)^2 + 1}\right]^2\right\}. \quad (28)$$

Note that if $\Delta\eta$ is set equal to zero, Eq. (28) reduces to Eq. (22). The rest of the discussion will be devoted to using the above equations in model calculations.

III. MODEL CALCULATIONS

For the theoretical model and the formalism presented here, the target system on which the electron scatters could be an atom, a molecule or a solid. Here we perform a model calculation for metallic lanthanum and cerium that belong to the lanthanide group. We envisage an electron scattering process in which a $4d$-subshell electron is excited. An atom from this group in a metallic environment is usually modeled as triply ionized, so the ground state configurations for the lanthanum and cerium ions would be $4d^{10}4f^0$ and $4d^{10}4f^1$, respectively. This means that in Figs. 1(a)–1(c), the following assignments are made for the states with labels ϵ, i, and ϵ' as, $\epsilon \to \epsilon f$, $i \to 4d$, and $\epsilon' \to 4f$. The state $|E\rangle$ representing the incident electron is a plane wave that may be decomposed into its partial waves. Only the g- and f-partial waves can couple to the $\underline{4d}4f\epsilon f$-state. However, the higher partial wave provides larger numerical values to the matrix element $v_{\epsilon E}$. Thus an assignment of $E \to Eg$ is made for that state label. As a consequence, assignments of $k \to 4f$, $n \to nf$, and $m \to mg$ should be made for these state labels in Figs. 1(e)–1(h), 1(j), and 1(k). From Fig. 1(a), we get the matrix element $v_{\epsilon E}$ in terms of Slater integrals as

$$v_{\epsilon E} = 2\sqrt{3}R^1(\epsilon f4f;Eg4d) + 2(\sqrt{66}/11)R^3(\epsilon f4f;Eg4d) + 10(\sqrt{390}/143)R^5(\epsilon f4f;Eg4d). \quad (29)$$

From the angular momentum graph representing the self-energy $S_D(E)$ in Fig. 1(f), we get the interaction matrix element v_{nD}^2 from Fig. 2(a) in terms of Slater integral as

$$v_{nD}^2 = 6R^1(4f4d;4dnf)^2 + \frac{22}{63}R^3(4f4d;4dnf) + \frac{5000}{11979}R^5(4f4d;4dnf)^2. \quad (30)$$

Similarly, from the angular momentum graph representing the self-energy $S_D(E)$ in Fig. 1(k), we get the interaction matrix element $v_{ED}'^2$ from Fig. 2(b) in terms of Slater integrals

$$v_{ED}'^2 = 4R^1(4fnf;4dmg)^2 + \frac{24}{77}R^3(4fnf;4dmg)^2 + \frac{3000}{17303}R^5(4fnf;4dmg)^2. \quad (31)$$

Finally, from the self-energy Σ_{4d} for the angular momentum graph represented by Figs. 2(c) and 2(d), we get the interaction matrix element v_m^2 in terms of Slater integrals as

$$v_m^2 = \frac{44}{55}R^1(4f4f;4dmg)^2 + \frac{12}{77}R^3(4f4f;4dmg)^2 + \frac{8100}{121121}R^5(4f4f;4dmg)^2 - \frac{8}{35}R^1(4f4f;4dmg)R^3(4f4f;4dmg) - \frac{8}{77}R^1(4f4f;4dmg)R^5(4f4f;4dmg) - \frac{48}{847}R^3(4f4f;4dmg)R^5(4f4f;4dmg). \quad (32)$$

The expressions in Eqs. (29)–(32) above have been obtained using the rules for evaluating angular momentum graphs.[21] With the above explicit expressions for the matrix elements we proceed to get numerical values for the relevant parameters that are needed to calculate the various spectral lines in Sec. II.

The continuum E states have been calculated in the Hartree-Fock potential of the triply ionized ion of cerium. In the following discussion, the Slater integrals for cerium will be used for lanthanum as well. (While there is no $4f$-state in the ground configuration of lanthanum atom/ion, there is an available localized $4f$-state below the Fermi level whenever there is a vacancy in a $3d$- or $4d$-subshell.) Any of the E-dependent matrix elements that appear in the principal part summation/integration is slowly varying. We therefore represent any such function as $f(E)$ with its appropriate quadratic fit:

$$f(E) = a + bE + cE^2,\ E_0 \leqslant E \leqslant E_0 + \Delta. \quad (33)$$

Then its principal part summation/integration represented by $F(E)$ takes the analytic form:

$$F(E) = \sum_n{}' \frac{f(E_n)}{E_n - E} \to P\int \frac{f(\epsilon)}{\epsilon - E}dx = [a + bE + cE^2]\ln\left|\frac{\Delta + E_0 - E}{E_0 - E}\right| + \Delta[b + c(\Delta/2 + E)]. \quad (34)$$

The contributions from the logarithmic component would be small. In the above Δ reflects the $\underline{4d}4f^N$-multiplet width for La ($N=1$) and Ce ($N=2$). The energy E_0 is the $4d \to 4f$ excitation energy. The parameters E_0 and Δ may be taken from experiment or multiplet calculations,[22] as displayed in Table I. With these values, any E-dependent quantity will be evaluated at some mean energy $\bar{E} = E_0 + \Delta/2$, say. In such a situa-

TABLE I. Computed q-values and ratios of autoionizing line widths to total line widths in the ring and ladder channels as described in the text.

Elements (configuration)	E_0[a] (eV)	Δ[a] (eV)	q	γ	q'	γ'
La ($4\underline{d}4f$)	97.2	19.8	−0.548		−0.0565	
Ce ($4\underline{d}4f^2$)	101.8	23.8	−0.521	0.950	−0.0628	0.783

[a]Data extracted from Ref. 22.

tion, the logarithmic contribution in Eq. (34) vanishes and we get for $F(\overline{E})$ the simple expression

$$F(\overline{E}) = \Delta[b + c(\overline{E} + \Delta/2)]. \tag{35}$$

Thus from Eqs. (7a) and (15a), the computed values of $q(\overline{E})$ and $q'(\overline{E})$ are presented in Table I, together with the values of γ and γ' that have been calculated using Eqs. (18) and (35).

IV. RESULTS AND DISCUSSION

In Fig. 3, the curve labeled (a) represents the theoretical line shape for Ce calculated using the complete expression defined by Eq. (28), with the appropriate parameters from Table I. The slowly varying nonresonant excitation matrix element $v^2_{\epsilon E}$ has been excluded. The corresponding theoretical curve for La using Eq. (28) with $\gamma = \gamma' = 1$ is similar in shape to the Ce curve with subtle differences in the resonance peaks and widths. Rather than comparing their relative line shapes, we have instead calculated the ratio of the line shape of Ce to La to reveal any elusive differences. The result of this ratio in which the La line shape was first normalized to the Ce peak is the curve labeled (b) in Fig. 3. The curve is troughlike with suppressed ridges. The flattened ridges approach the expected theoretical constant value of unity far away from the zero energy-loss regions. The width of the trough is ~3 eV. The curve labeled (c) is the experimental ratio of electron energy-loss spectra of Ce and La.[23] In computing this ratio the experimental data abscissas were translated so that their decreasing portions, i.e., their peak to trough portions are coincident as was done in Ref. 14. The well-shaped distribution of the computed data points was then fitted to a biphasic function so that the experimental trough minimum was aligned with the theoretical one in energy. We observe that the curve for the experimental ratio is also troughlike, but unlike the theoretical one, the ridges are pronounced. The width of the trough is ~8 eV.

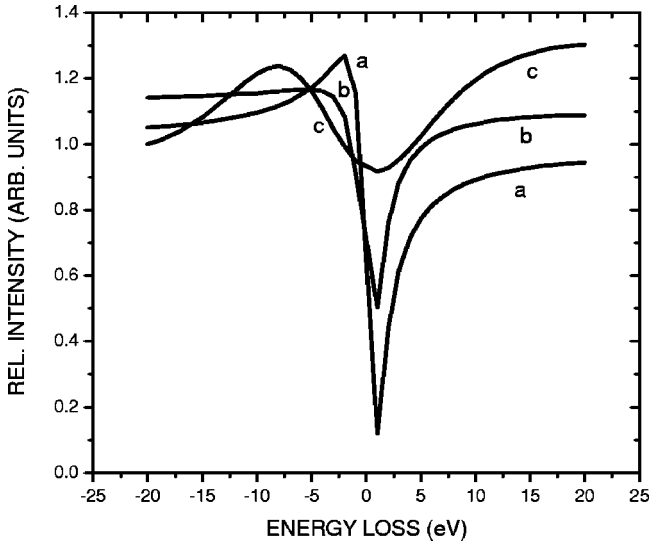

FIG. 3. Comparison of theoretical line shapes for metallic La and Ce with experiment: (a) The calculated full line shape for Ce; (b) ratio of the calculated full line shape for Ce to that of La; (c) electron energy-loss intensity ratio of Ce to La, computed from experimental data (Ref. 23).

While the general trend in the theoretical curve is found in the experimental one, there are two major discrepancies. The first is the pronounced ridges in the experimental curve as mentioned above. The second is the width of the experimental curve which is ~5 eV larger than the theoretical one. The former dissimilarity in the theoretical ratio arises mainly because spin-orbit interactions are not included in the theoretical formulation, while electron-energy and absorption spectra are known to be strongly dependent on spin-orbit effects.[22,24] The cause for the latter dissimilarity is inherent in calculated atomic-based theoretical resonance scattering spectra whose widths are typically narrower than those from experiment.[25] Notwithstanding the above remarks, the overall agreement of theory with experiment is fair to good.

Figure 4 is presented to elucidate the importance of the interaction parameter $\Delta\eta$. In the figure we make comparison of only theoretical line shapes of Ce with La along the lines as was done in Fig. 3. Figure 4(a) and 4(b) are the same as Fig. 3(a) and 3(b), respectively. Figure 4(c) is the ratio of the line shape of Ce to La using Eq. (28), but in the case of La, γ is set equal to zero to indicate that only contributions from ladder diagrams are retained from the expression. The resulting expression for La that is dependent on the parameter $\Delta\eta$ is numerically approximate to unity for all η-values. As a result this ratio is indistinguishable from the Ce line shape of Fig. 3(a)—hence the reason the curve bears the two labels "a, c." Figure 4(d) is the calculated line shape of Ce to La, again using Eq. (28), but this time it is γ' that is set equal to zero for La to indicate retention of only contributions from ring diagrams. The resulting expression for La is independent of the parameter $\Delta\eta$, and the curve for the ratio is highly resonant. (The maximum of this curve is 4.9 units occurring at the energy loss of −2 eV) This curve is contrasted with Fig. 4(e), which is the ratio of the Ce line shape defined by Eq. (28) to the La line shape defined by the Fano expression of

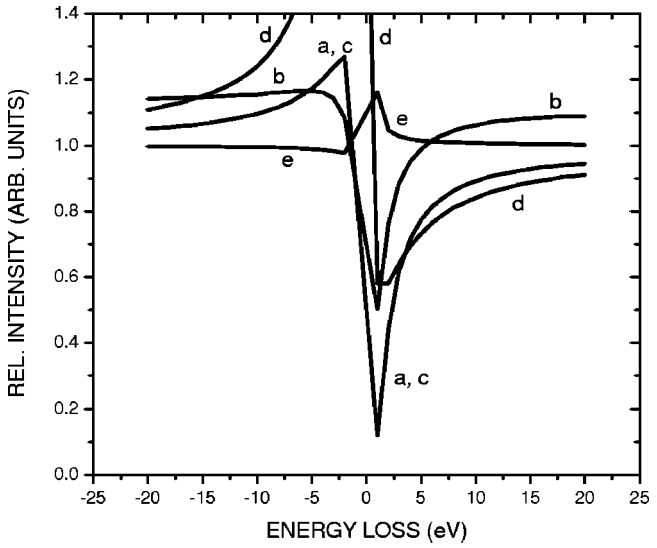

FIG. 4. Comparison of theoretical line shapes of Ce with La: (a) same as in Fig. 3(a); (b) same as in Fig. 3(b); (c) ratio of the calculated full line shape of Ce to La (including only ladder contributions); (d) ratio of the calculated full line shape of Ce to La (including only ring contributions); (e) ratio of the calculated full line width of Ce to La [Eq. (23)].

Eq. (23), i.e., due to contributions emanating from only ring diagrams assuming nonexisting ladder diagrams. We note that Eq. (23) is independent of $\Delta\eta$ and Fig. 4(e) also shows a resonance but not as pronounced as the one in Fig. 4(d). The point being made through Fig. 4 is that while the retention of only ring diagrams gives spurious picture for the ratio, its inclusion in the formalism is necessary to provide the needed interference between the autoionizing and characteristic channels to produce the troughlike semblance for the ratio to better compare with experiment. We note also that although retaining only ladder diagrams produces a somewhat troughlike picture for the ratio in Fig. 4(c) or equivalently in Fig. 3(a), it does not compare better with the experimental features than what Fig. 4(b) or Fig. 3(b) does.

Finally, the relative insignificance of ring to ladder diagrams can be seen as follows. The leading contribution to the excitation amplitude from ladder diagrams comes via Figs. 1(a) and 1(c) that are first order in Coulomb interaction while the leading contribution from the ring diagrams via Fig. 1(b) is second order in Coulomb interaction. Consequently, contributions from ring diagrams to core-electron impact excitation spectrum would be smaller than those from ladder diagrams. In instances where the diagrammatic RPA has been used with success, the exchange or ladder diagrams are treated as corrections to ring diagrams, and sometimes neglected altogether.[7–10] Also, as has been remarked in the RPA treatment for the charge fluctuation in metals using the Hubbard model, ladder graphs contribute more to the energy of the electrons, but little to their dynamic properties such as correlation.[26] Thus the minimal dynamic effects exhibited rather by ring diagrams in comparison to ladder diagrams is a novel observation manifested only in doing RPA with respect to core-electron impact excitation in metals.

The final theoretical expressions of Sec. II may be used to approximately fit experimental electron energy-loss data with trial and error choices of the parameters γ, γ', q, and q' such that $0 \leqslant \gamma,\ \gamma' \leqslant 1$. But as the foregoing discussion has indicated, for any meaningful fit, $\Delta\eta$ would have to be considered as well. The Fano parameters q and q' can also take on positive values, as would be the case if the core transition had been $2p \rightarrow 3d$ instead, as analyzed in Ref. 14. The formulation presented here may be extended to the transition metals. However, two philosophical difficulties present themselves. One is some proper decomposition of the perturbation diagrams for the 3*d*-open shell system or wide bands, and the other is the appropriate wave functions to be used for the 3*d*-states in numerical computations. Work in this direction is in progress. To summarize, we have extended the hybrid model that was based on ladder diagrams of diagrammatic perturbation theory to include ring diagrams as well, thereby providing a coherent random-phase approximation approach to electron scattering in solids.

ACKNOWLEDGMENT

The author wishes to thank Kent State University's Research Council for partial support.

*Electronic address: nuroh@salem.kent.edu

[1] R. Kubo, J. Phys. Soc. Jpn. **12**, 570 (1957); *Lectures in Theoretical Physics* (Wiley-Interscience, New York, 1959), Vol. I, pp. 120–123.

[2] See, for example, S. Doniach and E. H. Sondheimer, *Green's Functions for Solid State Physicists* (Benjamin, Reading, 1974), pp. 144–146.

[3] J. Hubbard, Proc. R. Soc. London, Ser. A **276**, 238 (1963); **277**, 237 (1964); **281**, 401 (1964).

[4] In Ref. 2, pp. 158–165.

[5] See, for example, A. L. Fetter and J. D. Walecka, *Quantum Theory of Many-Particle Systems* (McGraw-Hill, New York, 1971), pp. 154–156.

[6] In Ref. 5, pp. 131–139.

[7] M. Ya Amusia, N. A. Cherepkov, and L. V. Chernysheva, Sov. Phys. JETP **33**, 90 (1971).

[8] G. Wendin, J. Phys. B **3**, 466 (1970).

[9] G. Wendin, Phys. Rev. Lett. **53**, 724 (1984).

[10] G. Wendin and N. Kerr Del Grande, Phys. Scr. **32**, 286 (1985).

[11] A. Zangwill and P. Soven, Phys. Rev. A **21**, 1561 (1980).

[12] K. Nuroh, M. J. Stott, and E. Zaremba, Phys. Rev. Lett. **49**, 862 (1982).

[13] K. Nuroh, Phys. Scr. **56**, 56 (1997).

[14] K. Nuroh, Phys. Rev. B **66**, 155126 (2002).

[15] J. L. Dehmer, A. F. Starace, U. Fano, J. Sugar, and J. W. Cooper, Phys. Rev. Lett. **26**, 1521 (1971).

[16] A. F. Starace, Phys. Rev. B **5**, 1773 (1972).

[17] L. C. Davis and L. A. Feldkamp, Phys. Rev. B **23**, 6239 (1981).

[18] L. S. Cederbaum, W. Domcke, J. Schirmer, and W. von Niessen, Phys. Scr. **21**, 481 (1980).
[19] I. Lindgren and J. Morrison, *Atomic Many-Body Theory* (Springer-Verlag, New York, 1982), pp. 238–241.
[20] U. Fano, Phys. Rev. **124**, 1866 (1961).
[21] In Ref. 19, pp. 80–84.
[22] J. Sugar, Phys. Rev. B **5**, 1785 (1972).
[23] G. Strasser, G. Rosina, J. A. D. Matthew, and F. P. Netzer, J. Phys. F: Met. Phys. **15**, 739 (1985).
[24] K. Nuroh, Phys. Scr. **61**, 589 (2000).
[25] See, for example, Ref. 24, p. 593.
[26] Gerald D. Mahan, *Many-Particle Physics* (Kluwer Academic/ Plenum Publishers, New York, 2000), p. 411.